ADVANCED ENERGY MATERIALS
www.advenergymat.de

The (In)Stability of Heterostructures During the Oxygen Evolution Reaction

Indranil Mondal, J. Niklas Hausmann, Stefan Mebs, Shweta Kalra, Gonela Vijaykumar, Konstantin Laun, Ingo Zebger, Sören Selve, Holger Dau, Matthias Driess,* and Prashanth W Menezes**

The urgent need for efficient oxygen evolution reaction (OER) catalysts has led to the development and publication of many heterostructured catalysts. The application of such catalysts with multiple phases tremendously increases the material design dimensions, and numerous interface-related effects can tune the OER performance. In this regard, multiple of these heterostructured electrodes show remarkable OER activities. However, it is not clear if these carefully designed interfaces remain under prolonged OER conditions. Herein, a molecular approach is used to synthesize four different nickel-iron phosphide (heterostructured) materials and deposit them on fluorine-doped tin oxide and nickel foam electrodes. The OER performance of the eight electrodes and the reconstruction of the four materials is investigated by in-situ spectroscopy after one day of operation, enabled by a freeze-quench approach. The most active electrode is also applied under industrial OER conditions and for the value-added oxidation of alcohols to ketones. Before catalysis, this electrode comprises crystalline 4 nm nickel phosphide particles on an amorphous iron phosphide matrix. However, after 24 h, a homogenous nickel-iron oxyhydroxide phase has formed. This work questions to which extent the design of heterostructures is a suitable strategy for non-noble metal OER catalysis.

1. Introduction

Hydrogen is a potential carbon-neutral fuel and an important commodity chemical.[1] It can be sustainably produced through electrocatalytic alkaline water splitting. However, the efficiency of water splitting is mainly hampered by the unsatisfactory performance of oxygen evolution reaction (OER) catalysts catalysts.[2] Unfortunately, the design opportunities of OER-catalysts are strongly limited by the widely reported reconstruction of most materials into similar transition metal oxyhydroxides during operation.[3–6] In this regard, heterostructured electrodes offer more design opportunities than single-phase catalysts and have often achieved outstanding performances.[7–13] Previous reports on such systems have raised several interface-related hypothesis for their performance such as interfacial electron redistribution,[14] a Mott-Schottky

I. Mondal, S. Kalra, G. Vijaykumar, M. Driess, P. W Menezes
Department of Chemistry
Metalorganics and Inorganic Materials
Technische Universität Berlin
Straße des 17. Juni 135, Sekr. C2, 10623 Berlin, Germany
E-mail: matthias.driess@tu-berlin.de;
prashanth.menezes@mailbox.tu-berlin.de

I. Mondal
School of Chemistry
Indian Institute of Science Education and Research Thiruvananthapuram
Kerala 695551, India

The ORCID identification number(s) for the author(s) of this article can be found under https://doi.org/10.1002/aenm.202400809

DOI: 10.1002/aenm.202400809

J. N. Hausmann, P. W Menezes
Materials Chemistry Group for Thin Film Catalysis–CatLab
Helmholtz–Zentrum Berlin für Materialien und Energie
Albert-Einstein-Str. 15, 12489 Berlin, Germany

S. Mebs, H. Dau
Fachbereich Physik
Freie Universität Berlin
Arnimallee 14, 14195 Berlin, Germany
E-mail: holger.dau@fu-berlin.de

K. Laun, I. Zebger
Department of Chemistry
Physical Chemistry/Biophysical Chemistry
Technische Universität Berlin
Straße des 17. Juni 135, Sekr. PC14, 10623 Berlin, Germany

S. Selve
Center for Electron Microscopy (ZELMI)
Technische Universität Berlin
Straße des 17. Juni 135, Sekr. KWT2, 10623 Berlin, Germany

junction with local charge polarization,[15] interruption of the interfacial water dipole rearrangement,[16] or other synergistic effects of the interface comprising phases.[11] However, it has not been proven that the interfaces between non-noble-metal-based (oxyhydroxide) phases remain during OER, especially when operated for prolonged times such as a day. If the as-prepared phases or the reconstructed oxyhydroxides intermix, the reason for the increased activity does not originate from the interface. Thus, a profound in-situ investigation after long operating times on a systematic series of heterostructures is required.

The nickel-iron phosphide system has shown promising performances for the OER and organic oxidation reactions.[19,20] where phosphorus is a sacrificial reagent that helps to create a high-surface-area, defect-rich, nickel-iron oxyhydroxide phase in a reconstruction process.[3–6] This well-investigated system is ideal for studying the behavior of different heterostructures and their interfaces during electrocatalysis. A judicious choice to form the required heterostructures is the molecular precursor approach.[21] This approach requires only modest temperatures, leads to the controlled formation of monodispersed nanoparticles, is suitable for bimetallic systems, and can yield heterostructures with unique interfaces in a single step.[21] To investigate this system in depth, we chose an in-situ freeze-quench approach followed by Raman and X-ray absorption spectroscopy[22] and paired it with high resolution elemental scanning electron microscopy mappings. The freeze-quench approach is particularly suitable, as it allows us to precondition the various samples in non-in-situ cells for 24 h before measurement. Such a long preconditioning of various samples is otherwise challenging in-situ cells, especially for synchrotron-based methods, considering the availability of in-situ setups and beamtime. However, we think that a combination of these in-situ methods and long preconditioning times is required to reveal the long-term destiny of heterostructured systems.

Herein, using a molecular precursor approach, we obtain crystalline nickel phosphide nanoparticles (Ni_2P), amorphous iron phosphide (FeP_x, $x \approx 1.7$), a physical mixture (PM) of both phases (NiFe:PM), and a unique heterostructure from a single source precursor (SSP), where ≈4 nm Ni_2P particles are homogeneously embedded into a FeP_x ($x \approx 0.43$) matrix (NiFe:SSP). These four materials are loaded on two electrode substrates, fluorine-doped tin oxide (FTO) and nickel foam (NF), yielding additional interfaces and, in total, eight electrode systems. These systems were applied for the OER and their reconstruction was monitored after 24 h. While the reconstructions of the phosphides to corresponding oxyhydroxides and the activity enhancement due to the Ni-Fe bimetallic functions are noteworthy, this manuscript focuses on the (in)stability of the interfaces, e.g., mixing of the different transition metal oxyhydroxide phases. We reveal that the material's interfaces and transition metal distribution enormously change and that the interface between electrode substrate (fluorinated tin oxide (FTO) or nickel foam (NF)) and the catalyst can be critical. The NiFe:SSP system, which was also applied under industrially relevant conditions (65 °C, 6 M KOH, 500 mA cm^{-2}, 80 h) and for the selective dehydrogenation of alcohols, fully reconstructs into a phase with homogeneous nickel-iron distribution yielding 10 mA cm^{-2} at merely 195 ± 5 mV overpotential. The homogeneous distribution shows that no interface between a monometallic nickel and monometallic iron phase remains in the highly active catalyst. Thus, the previously raised interface-based hypothesis for the high activity of such systems must be reconsidered.

2. Results

2.1. Synthesis and Structure of the Transition Metal Phosphide Precatalysts

Three different precursors were used for the transition metal phosphide synthesis: a nickel dicyclooctadiene ($Ni(cod)_2$), iron 1,1′-bis(diphenylphosphino)ferrocene ($Fe(dppf)_2$), and [$Fe(dppf)_2Ni(cod)$] (**Figure 1**). All three molecular precursors were heated to 270 °C in oleylamine with trioctylphosphine as surfactant, resulting in the formation of black powders. For $Ni(cod)_2$ and $Fe(dppf)_2$, triphenylphosphine (PPh_3) was added as a phosphorus source, and the obtained materials are called FeP_x and Ni_2P. For $Fe(dppf)_2Ni(cod)$, no phosphorus source is required due to the already existing Ni—P bonds in the molecular complex. Thus, $Fe(dppf)_2Ni(cod)$ is a single-source precursor, and the obtained material is called NiFe:SSP. The fourth material is a physical mixture of FeP_x and Ni_2P in the ratio of 1:2 (NiFe:PM).

The purity, surface electronic properties, and morphology of all as-prepared materials were investigated by powder X-ray diffraction (PXRD), scanning electron microscopy (SEM) with energy dispersive X-ray (EDX) mappings, transmission electron microscopy (TEM) with selected area electron diffraction analysis (SAED), scanning transmission electron microscopy (STEM), X-ray photoemission spectroscopy (XPS), and inductively coupled plasma atomic emission spectroscopy (ICP-AES, see Figures S1–S8, Supporting Information for all data). **Figure 2** shows the most relevant TEM/STEM data of all four compounds. This analysis shows that Ni_2P comprises phase-pure, crystalline (JCPDS: 03–953, *P*321), monodispersed Ni_2P nanoparticles with ≈20 nm diameter (Figure 2a; Figures S5,S6, Supporting Information). FeP_x ($x \approx 1.7$) is amorphous with a homogenous distribution of iron and phosphorus and has a sheet-like morphology (Figures S7,S8, Supporting Information). In the physically mixed sample, NiFe:PM, the Ni_2P particles reside partly on top and partly next to the FeP_x phase (Figure 2c). The single-source-precursor-derived sample, NiFe:SSP, comprises an amorphous FeP_x matrix ($x \approx 0.43$) with embedded ≈4 nm small, spherical Ni_2P nanoparticles (Figure 2d–j; Figure S3, Supporting Information). The Ni to Fe ratio of NiFe:SSP is 2 to 1. (Figures S2,S3, Supporting Information).

2.2. Electrocatalytic Investigation of the Oxygen Evolution Reaction Activity of the Four Phosphides on Fluorine-doped Tin Oxide (FTO) and Nickel Foam (NF)

2.2.1. Cyclic voltammetry (CV) and Impedance Spectroscopy

The four different phosphides shown in Figure 1 as well as a $Ni_{0.7}Fe_{0.3}OOH$ and NiOOH reference (see Figures S9,S10 (Supporting Information) for their characterization) were electrophoretically deposited without binder on FTO glass plates

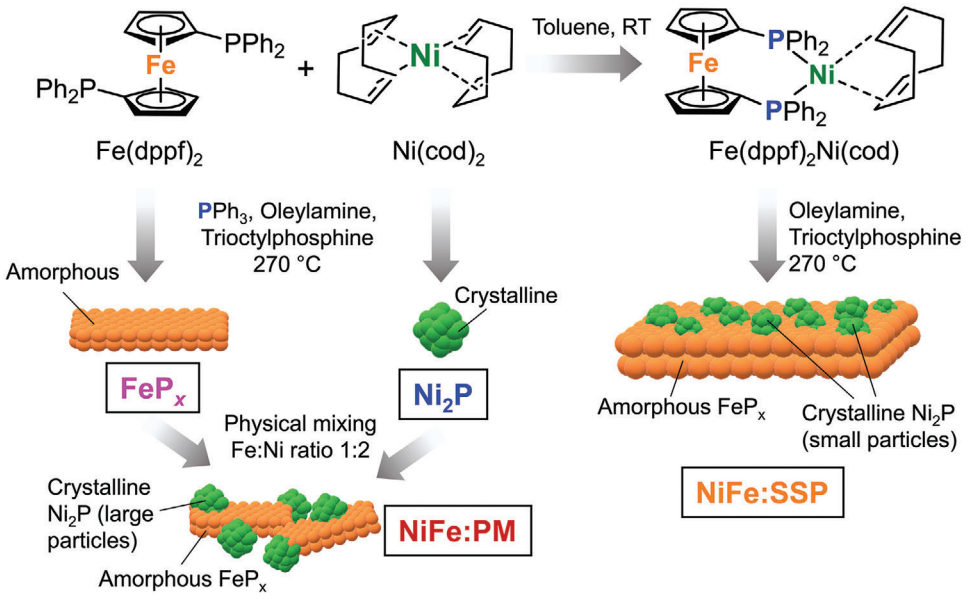

Figure 1. Synthesis of the four different transition metal phosphide materials, FeP_x, Ni_2P, NiFe:PM, and NiFe:SSP (PM and SSP are abbreviations for physical mixture and single-source precursor), investigated herein. The color code (pink, blue, red, orange) is retained throughout this manuscript and its Supporting Information. At the top, the synthesis of the single-source precursor (SSP), $Fe(dppf)_2Ni(cod)$ is shown. The steps below show the phosphide formation using the three different molecular precursors. The fourth compound is a physical mixture (PM) of FeP_x and Ni_2P in the Fe to Ni ratio of 1:2 (NiFe:PM).

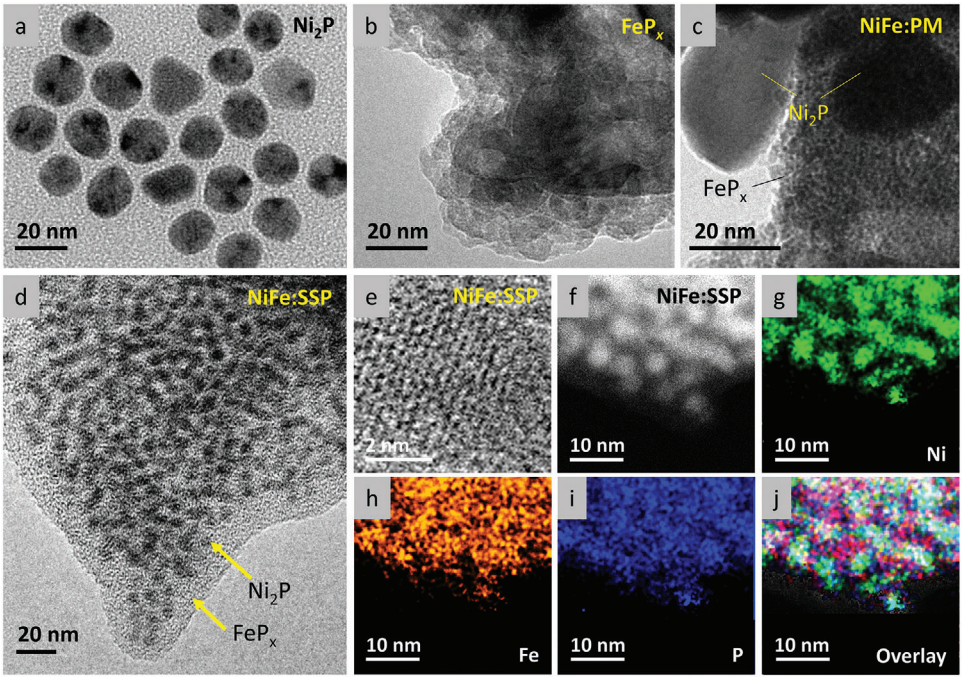

Figure 2. TEM data of the four herein investigated materials whose synthesis and abbreviations are described in Figure 1. The as-prepared Ni_2P a) comprises 20 nm large, monodispersed, crystalline nanoparticles, whereas the as-prepared FeP_x b) comprises amorphous sheet-like structures. These two different nanostructures are clearly visible in the physical mixture c). Additional characterizations for these three compounds can be found in Figures S1–S8 (Supporting Information). Images d–j show TEM and STEM data with respective elemental mappings of the SSP-derived sample, revealing that ≈4 nm large nickel phosphide nanoparticles are embedded in an amorphous iron phosphide matrix (Figure S3, Supporting Information for the EDX spectrum). The colors represent the spatial distribution of Ni (green), Fe (orange), and P (blue).

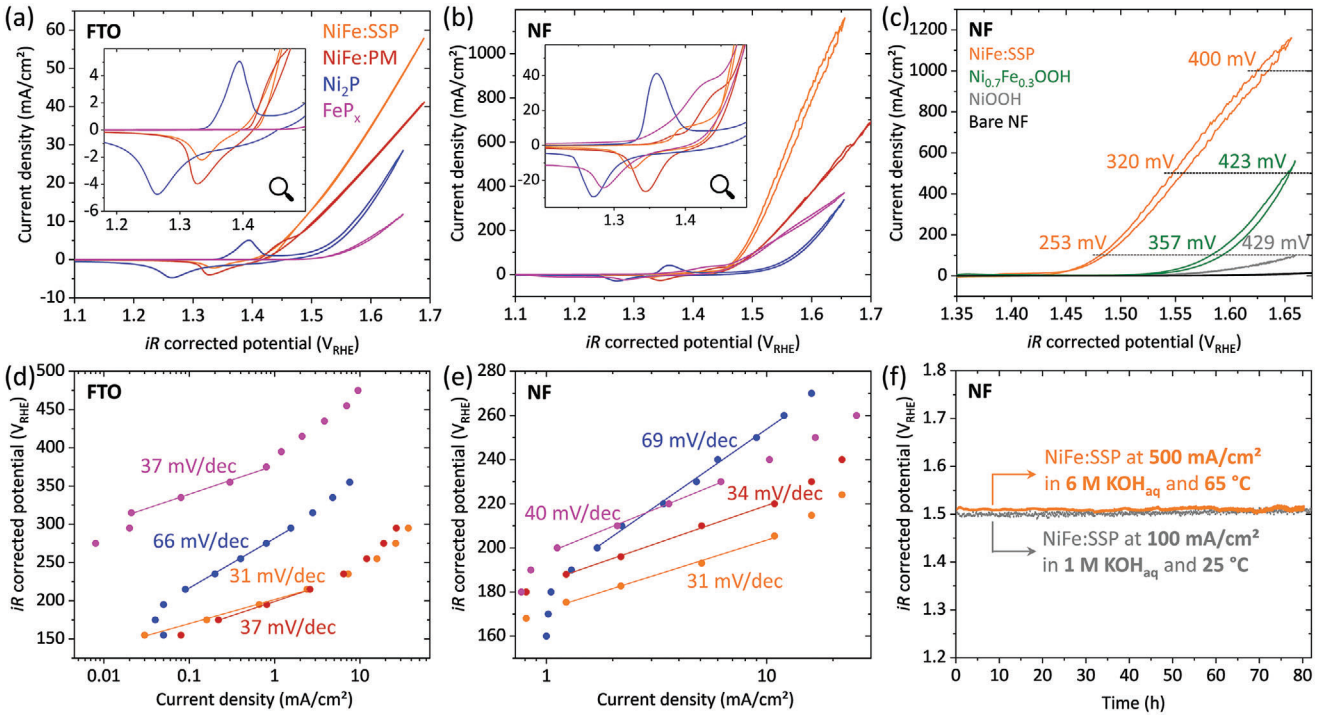

Figure 3. Electrochemical OER data in 1 M KOH at 25 °C of the four samples shown in Figure 1 and two nickel(-iron) oxyhydroxide reference samples deposited without binder on fluorine-doped tin oxide glass plates (FTO, loading 0.4 mg cm^{-2}) and nickel foam (NF, loading 0.8 mg cm^{-2}). Cyclic voltammograms at a scan rate of 5 mV s^{-1} of the samples on FTO a) and NF b) with an inset showing a zoom into the redox peak region. c) shows the CV of the most active sample (NiFe:SSP on NF) and the two nickel(-iron) oxyhydroxide reference samples with their respective overpotentials. Tafel plots based on steady-state measurements with holding times of 2 min at each respective potential of the samples on FTO d) and NF e). f) shows long-term stability measurements (chronopotentiometry) of the most active NiFe:SSP on NF sample in typical academic testing conditions (100 mA cm^{-2}, 1 M KOH, 25 °C) and industrially relevant ones (500 mA cm^{-2}, 6 M KOH, 65 °C).

(loading 0.4 mg cm^{-2}, see Figures S11–S14, Supporting Information) and NF (loading 0.8 mg cm^{-2}, see Figure S13, Supporting Information). Before any electrochemistry data was acquired, all samples were cycled around 30 times until a stable current response was obtained. Cyclic voltammograms (**Figure 3**a,b) and steady-state chronoamperometry data (Figure 3d,e) in aqueous 1 M KOH (pH 13.89)[23] of the four transition metal phosphide materials reveal that NiFe:SSP has the lowest overpotential at 10 mA cm^{-2} (η_{10}) of all electrodes on FTO (248 ± 4 mV) and NF (195 ± 6 mV). These overpotentials are substantially lower than the ones of $Ni_{0.7}Fe_{0.3}OOH$ and NiOOH nanoparticles (Figure 3c; Figure S15, Supporting Information). The η_{10} order on FTO is NiFe:SSP<NiFe:PM<Ni_2P<FeP_x. To assess the effect of crystallinity, we synthesized crystalline Fe_2P and physically mixed it with crystalline Ni_2P, maintaining a similar Ni-Fe ratio as in NiFe:SSP (see Figure S16, Supporting Information). Interestingly, this sample showed a substantially worse OER activity compared to NiFe:SSP and NiFe:PM (Figure S17, Supporting Information), despite exhibiting a similar Ni-redox activity. This suggests that the crystallinity of the precatalyst also plays a crucial factor. For the four sample of Figure 1, on NF the activity order remains the same, except that FeP_x becomes more active and has a lower η_{10} than Ni_2P and a similar one to NiFe:PM. Surface area normalization does not change this order on any of the substrates (Figures S18,S19, Supporting Information). Furthermore, the NF η_{100} values match the η_{10} ones on FTO, meaning that the NF substrate increases the activity (current density at the same overpotential) roughly by a factor of ten. Again, this is not the case for FeP_x, where this factor is above 100. The distinct behavior of FeP_x indicates that the NF is not only an inert substrate but also chemically interacts with the FeP_x, likely by forming $NiFeO_xH_y$ (see also Note S3, Supporting Information). The activity trends of all samples have also been investigated by impedance measurements at 1.50 V_{RHE}, whose simulations reveal that the charge transfer resistances follow the same trend as the overpotentials (Figure S20, Supporting Information).

2.2.2. Tafel Analysis

Tafel plots (Figure 3d,e) from steady-state data were acquired to get further insights into the activity trends. It has been shown that the nickel-iron ratio strongly affects the Tafel slope. For rigorously iron-free nickel-based catalysts, Tafel slopes of 70–110 mV dec^{-1} have been observed.[24–30] For monometallic iron-based catalysts, insufficient electron conductivity can disturb the Tafel slope measurements, and potentiodynamic methods have found slopes above 100 mV dec^{-1}.[29,30] In contrast, steady-state methods have found Tafel slopes of 30–46 mV dec^{-1} and strong substrate effects, as only the iron centers close to the conducting electrode substrate are anodically wired and can participate in the OER.[24,31] Herein, for Ni_2P, tested in non-iron-purified

electrolyte Tafel slopes of 66 and 69 mV dec^{-1} on FTO and NF, respectively, have been measured, which is in line with previously published pure nickel oxyhydroxide operated in non-purified electrolytes.[29,30] The difference between the FTO and NF sample is within the standard deviation of our Tafel data, ±3 mV dec^{-1}. Thus, for Ni_2P, the substrate does not significantly change the reaction mechanism and nature of the active sites. FeP_x has the second-highest Tafel slope with 37–40 mV dec^{-1}, which is in line with steady-state measurements of monometallic iron-based samples.[31] The lowest Tafel slopes are observed for the nickel and iron-containing precatalysts, with 34–37 mV dec^{-1} for the physical mixture and 31 mV dec^{-1} for the single source precursor derived one. Both show no substrate-dependence of the Tafel slope and the lower value for NiFe:SSP indicates that its nickel-to-iron ratio and distribution is ideal, while for NiFe:PM likely either too much iron or too much nickel is present in the active structures. As both samples have the same nickel-to-iron ratio, the distribution of both elements must be the critical factor.

2.2.3. Stability at Industrially Relevant Conditions (6 M KOH, 65 °C) and Application for an Organic Oxidation Reaction (Hybrid Water Electrolysis)

The stability of all catalysts has been investigated for 24 h (Figure S21, Supporting Information) at 10 mA cm^{-2} and they all show stable performance. For the most active electrode (NiFe:SSP on NF), long-term stability measurements in typical academic testing conditions (100 mA cm^{-2}, 1 M KOH, 25 °C) and industrially relevant ones (500 mA cm^{-2}, 6 M KOH, 65 °C) have been performed (Figure 3f). In both conditions, the overpotential remains stable over the test period of 80 h. In the industrially relevant conditions, a five times higher current density is reached without the requirement of additional overpotential compared to the academic testing conditions.

To further show the applicability of the NiFe:SSP on NF, we performed an organic oxidation reaction, which can replace the economically non-viable OER (hybrid water electrolysis). This organic oxidation reaction produces ketones from secondary alcohols and requires less potential than the OER (see Note S1 in the supporting information). Thus, it produces valuable ketones instead of the OER's low-value dioxygen and additionally lowers the overall energy costs of hydrogen production. The electrochemical and analytical data are shown in Figures S22–S26 (Supporting Information). Three alcohols were used as test substrates and Faradaic efficiencies and ketone yields between 81–96% were achieved.

2.3. The Reconstructed Phases of the Four Nickel-Iron Phosphide Heterostructures

2.3.1. X-ray Diffraction and Scanning Electron Microscopy

Transition metal phosphides have been shown to reconstruct into oxyhydroxides during the OER.[3,5,32] Herein, we especially investigate if the initial heterostructures and their interfaces remain after catalysis for 24 h or if and how they affect the reconstructed phases. The characterizations are mainly performed on the phosphides deposited on FTO, as especially in-situ X-ray absorption spectroscopy (XAS) and Raman measurements on NF are challenging. Before all characterization, the samples were cycled until a stable current response was obtained and treated for 24 h at 10 mA cm^{-2} (Figure S21, Supporting Information). XRD data of the four electrodes after the treatment show only the reflexes of FTO (Figure S27, Supporting Information shows the representative NiFe:SSP/FTO data). Thus, the initially crystalline phases are fully reconstructed into amorphous or nanocrystalline structures. SEM-EDX analyses of all films show that only traces of phosphorous remain and severe incorporation of oxygen (Figures S28–S31, Supporting Information).

2.3.2. Quasi-In-Situ Raman Spectroscopy and the Effect of Time and Precursor Type on the Reconstruction

The XRD and electron microscopy data fit the previously observed formation of amorphous oxyhydroxides. (Iron-incorporated) nickel oxyhydroxides show two characteristic Raman bands for the bending δ(Ni-O) (≈480 cm^{-1}) and stretching ν(Ni-O) (≈560 cm^{-1}) vibrations (**Figure 4a**).[25,26,28] These two bands without additional peaks are present in the quasi-in-situ Raman spectra of NiFe:SSP, NiFe:PM, and Ni_2P acquired by freeze quenching the electrodes at 1.53 V_{RHE} after the 24 h pretreatment at 10 mA cm^{-2}. These bands reveal the formation of nickel(-iron) oxyhydroxides. This ratio is the lowest for Ni_2P (0.85), followed by NiFe:PM (1.25) and NiFe:SSP (1.5), indicating that Ni_2P has the least iron incorporated into the formed oxyhydroxide and NiFe:SSP the most. This is also consistent with the observation that SSP has the lowest and Ni_2P has the highest Tafel slope (Figure 3d,e). For the nickel-free FeP_x, we cannot identify any unambiguous signal originating from a pure iron (oxy)hydroxide, likely because of a low Raman scattering cross-section compared to nickel oxyhydroxides. Moreover, a highly amorphous nature might cause a further reduction of the Raman intensity. For the same reason, after OER, the FeP_x sample shows only very weak and broad signals at around 300 and 500 cm^{-1} (Figure S32, Supporting Information).[33] The ν/δ ratio has recently been proposed to correlate to the amount of incorporated iron and resulting structural disorder.[26]

Previous studies have found intact nickel and iron pnictide and chalcogenide phases during OER catalysis.[9,34,35] Thus, such heterostructures have been proposed to prevail and boost the OER activity. The data herein show that all four phosphide precursors are fully reconstructed. These different observations could be caused by different reconstruction times used in the literature compared to the herein exceptionally long 24 h prior to the in-situ measurement. We therefore investigated the time dependence of the reconstruction NiFe:SSP with quasi-in-situ Raman spectroscopy (Figure 4b). After 30 seconds, the Raman spectra already show very weak peaks in the 400–600 cm^{-1} region for the oxyhydroxides. The peak intensity of these peaks increases over time until they remain nearly unchanged after 20 min. In addition to these peaks, broad vibrational bands between 650–950 cm^{-1} are found. We assign these vibrations to the hydrated PO_x compounds of the electrochemical phosphide oxidation.[36–38] These peaks strongly increase in the first 5 min and then decrease again until they are absent at 30 min. From these observations, we

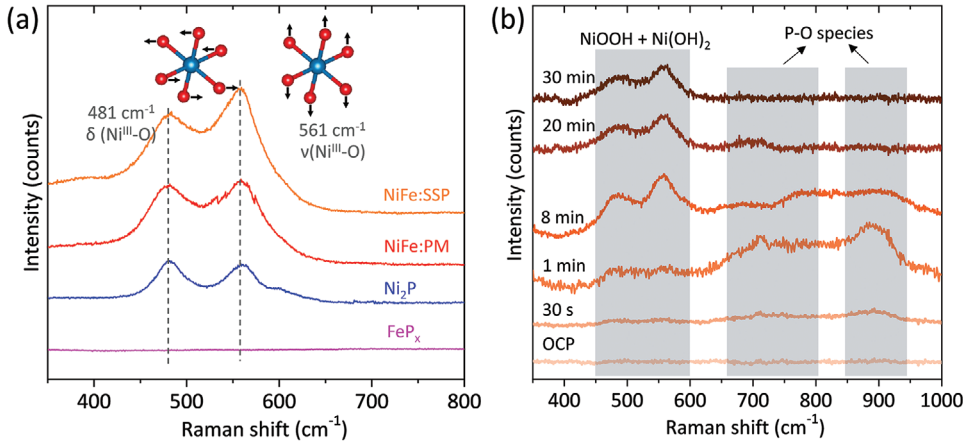

Figure 4. a) Quasi-in-situ Raman spectra of the four different samples (Figure 1) on FTO after 24 hours of OER-CP at 10 mA cm^{-2} and subsequent freeze-quenching at 1.53 V_{RHE}. The two typical vibrations for layered nickel (oxy)hydroxides are marked as grey dashed lines and visualized with the two octahedra (see Figure S32 (Supporting Information) for the spectrum of FeP_x during OER). b) Quasi-in-situ Raman spectra of NiFe:SSP/FTO film recorded at different times at 1.50 V_{RHE} to track the time-dependent reconstruction of the transition metal phosphides into nickel(-iron) oxyhydroxides and electrolyte soluble phosphate species.

deduce that the phosphide oxidation is completed after 30 min. Furthermore, SEM-EDX measurements reveal that after 30 min, no phosphorus is left in the NiFe:SSP sample (Figure S33, Supporting Information). The same measurements for NiFe:PM, Ni_2P, and FeP_x show that phosphorus is still present after 30 min. Thus, the phosphorus leaching is a function of time and phosphide precursor type.

2.3.3. Quasi-In-Situ X-ray Absorption Spectroscopy

By freeze quenching the electrodes (see ESI for details) during operation, quasi-in-situ XAS at the iron and nickel K-edges have been performed to investigate the oxidations states and local structures of the four (Figure 1) reconstructed (24 h at 10 mA cm^{-2}) electrodes. This approach allows us to condition all four samples for 24 h prior to the XAS measurements, which would be challenging in a real in-situ cell, considering the availability of beamtime and in-situ setups.

Quasi-in-situ X-ray absorption near edge structure (XANES) analysis reveals that the samples strongly oxidize during the OER, leading to oxidation states around and above three during electrocatalysis, consistent with the formation of (oxy)hydroxides. These (oxy)hydroxides are redox active, as shown by the reversible redox peaks of their CV's (Figure S34, Supporting Information). These redox peaks involve the nickel oxidation states II, III, and IV, with the main redox peak assignable to the transition from $Ni^{II}(OH)_2$ to $Ni^{III/IV}O_x(OH)_y$.[27,29,30] Consistent with its Pourbaix diagram, iron shows comparably little redox activity (high redox activity means that a high percentage of the Ni sites change their oxidation state), and it has been shown that the incorporation of iron into the layered nickel oxyhydroxide structure reduces the redox activity of nickel and lowers nickel's in-situ oxidation state.[27,29,30] Thus, a heterostructure with a monometallic nickel and a monometallic iron (oxy)hydroxide phase should show larger nickel oxidation state changes than a mixed nickel-iron (oxy)hydroxide phase. To investigate the nickel redox activity and its correlation with the nickel-iron mixing, in-situ XANES analysis at a potential below the redox peak (1.33 V_{RHE}) and above the redox peak (1.53 V_{RHE}, during the OER) was performed. This data shows a clear trend for the redox activity of nickel (the difference of the oxidation states at 1.53 and 1.33 V_{RHE} called $\Delta_{1.53\text{-}1.33VRHE}$) (**Table 1**, **Figure 5**). It is the largest (1.5) for Ni_2P, as it contains the least iron. For the PM sample, the redox activity is reduced by 20%, likely because some iron enters the redox active nickel phase. Note that both samples contain the same Ni_2P nanoparticles. Thus, this value should not be affected by surface area or other effects. The SSP sample shows only 60% of the redox activity, even though it has the highest BET surface area. Thus, the strong reduction of the redox activity is probably caused by iron incorporation into the redox active nickel phase.

The EXAFS data of the reconstructed phases were simulated with a model based on nickel(-iron) (oxy)hydroxides. These nickel(-iron) (oxy)hydroxides form a layered structure comprising edge-sharing [MO_6] octahedra, and the applied model considers three shells (M-O_a, M-M, and M-O_b, black rings **Figure 6a**) of this layered structure.[40] The total number of shells was six, as for every shell in the layered structure two distances (*R*-values) were considered, as the transition metal oxidation states within our samples vary between two and four, leading to different bond distances and thus *R*-values (Tables S1–S8, Supporting Information). For example, for the Ni-O_a bond, a short Ni-O_a (1.88–1.90 Å) bond distance for the oxidation states III and IV (present in γ-nickel oxyhydroxide) and a longer Ni-O_a (2.05–2.12 Å) bond distance for the oxidation state II (present in nickel hydroxide) was considered. Following this approach, we have also included a long and a short *R*-value for the M-M and M-O_b shells, whose respective coordination numbers (*N*-values) were restrained to be the same for all three short (M-O_a, M-M, M-O_b) and all three long shells, according to an ideal layered model (Figure 6a). For the monometallic iron sample, FeP_x, fits with this restrain were substantially worse (see Tables S5–S8 (Supporting Information) for fits with both models). This observation is reasonable, as monometallic iron, OER-derived oxyhydroxide phases are

Table 1. Bulk oxidation states of the four samples shown in Figure 1, determined through quasi-in-situ X-ray absorption near edge structure (XANES) analysis (Figures S35,S36, Supporting Information for details). The samples 1.33 V_{RHE} and 1.53 V_{RHE} have been deposited on fluorine-doped tin oxide glass plates (FTO), then reconstructed for 24 h at 10 mA cm^{-2}, and subsequently freeze quenched at 1.33 V_{RHE} or 1.53 V_{RHE}. $\Delta_{1.53\text{-}1.33VRHE}$ is the difference between the oxidation state at 1.53 V_{RHE} and 1.33 V_{RHE}. This difference should be roughly proportional to the redox activity of the sample determined from the integration of the reduction peak and shown in the last column (Figure S34, Supporting Information for details).

	Fe K-edge XANES oxidation states				Ni K-edge XANES oxidation states				CV redox peak integration [C cm^{-2}]
Sample	powder	1.33 V_{RHE}	1.53 V_{RHE}	$\Delta_{1.53\text{-}1.33VRHE}$	powder	1.33 V_{RHE}	1.53 V_{RHE}	$\Delta_{1.53\text{-}1.33VRHE}$	
Ni_2P	–	–	–	–	1.1	2.2	3.7	1.5	0.22
FeP	2.0	2.7	2.8	0.1	–	–	–	–	–
NiFe:PM	2.0	3.0	3.1	0.1	1.1	2.2	3.4	1.2	0.15
NiFe:SSP	2.2	3.1	3.1	0	0.5	2.8	3.4	0.6	0.08

structurally more versatile and do not only comprise edge-sharing octahedra.[41,42] As a whole, the suitability of these models shows that all reconstructed catalysts have evolved into layered oxyhydroxide phases.

Concerning the assignment of short and long *R*-values of the three shells to certain oxidation states, we note that their coordination numbers are also strongly affected by Jahn-Teller distortions, e.g., of low-spin iron(III). Thus, such an assignment is not straightforward, especially not for the M-M and M-O_b shells, whose *N*-values depend on multiple bond lengths and angles. Nevertheless, for the M-O_a *R*-value, which represents an M-O bond distance, semi-quantitative trends are observed. In this regard, Ni_2P and NiFe:PM show a dominant *N*-value of the long M-O_a shell (>5.5 vs <0.7 for the short one)[40] at 1.33 V_{RHE} (XANES oxidation state 2.2) and a dominant *N*-value of the short M-O_a shell (>4.4 vs <1 for the long one)[40] at 1.53 V_{RHE} (XANES oxidation state 3.4–3.7). For the less redox active NiFe:SSP, the short M-O_a shell's *N*-value is always dominant (>4.4, XANES oxidation state 2.8-3.4), and the long distance is not meaningful for the simulation of the data at 1.53 V_{RHE}. In contrast to nickel, iron shows almost no redox activity in the XANES measurements. This observation is also confirmed by the *N*-values of the short and long M-O_a shells, which are similar at 1.33 and 1.53 V_{RHE}. As iron is likely in an oxidation state of III, the population of a short and long M-O_a could also be caused by a Jahn-Teller distortion due to the unevenly occupied t_{2g} orbital. In total, the EXAFS populations confirm the XANES and CV oxidation state changes.

2.3.4. Scanning Transmission Electron Microscopy (STEM)

In-situ Raman and XAS have revealed that the amorphous phases that formed during the OER are nickel(-iron) oxyhydroxides. Thus, all four formed catalysts are structurally similar. However, their OER and redox activities are substantially different. This difference is caused by the different nickel and iron contents and the distributions of these elements in the four samples. To investigate the distribution in depth for the two samples with the same nickel and iron contents (NiFe:PM and NiFe:SSP), we performed high-resolution, element-specific STEM mappings (**Figure 7**). The mapping of NiFe:SSP reveals a homogeneous distribution of nickel, iron, and oxygen. Nothing of the initial heterostructure (Ni_2P nanoparticles on a FeP_x matrix) remains in terms of morphology and elemental distribution, and a single homogenous nickel-iron oxyhydroxide phase is formed. The mapping of NiFe:PM reveals that the original heterostructure changed completely into oxyhydroxides, and no monometallic iron or nickel phase or interphase remains. Only a few nickel-rich (but also iron-containing, at least in their near-surface region) spots that likely originate from the Ni_2P nanoparticles prevail. The absence of a monometallic nickel phase shows also the complete shift of the reduction peak of NiFe:PM compared to Ni_2P (Figure S34, Supporting Information). Furthermore, Figure 7b and Figure S39 (Supporting Information) show that NiFe:SSP forms a highly porous structure, which is ideal for exposing many active sites to the electrolyte and is probably caused by the

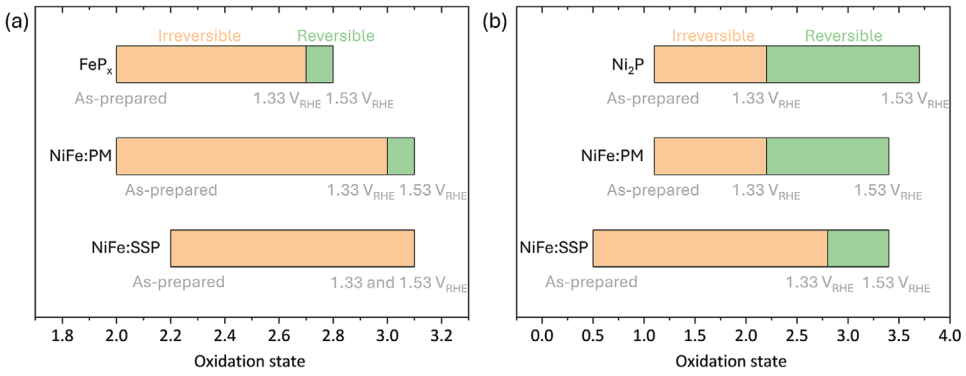

Figure 5. Floating bar diagrams visualizing the change in the oxidation states determined by XANES. a) based on Fe K-edge and b) based on Ni K-egde.

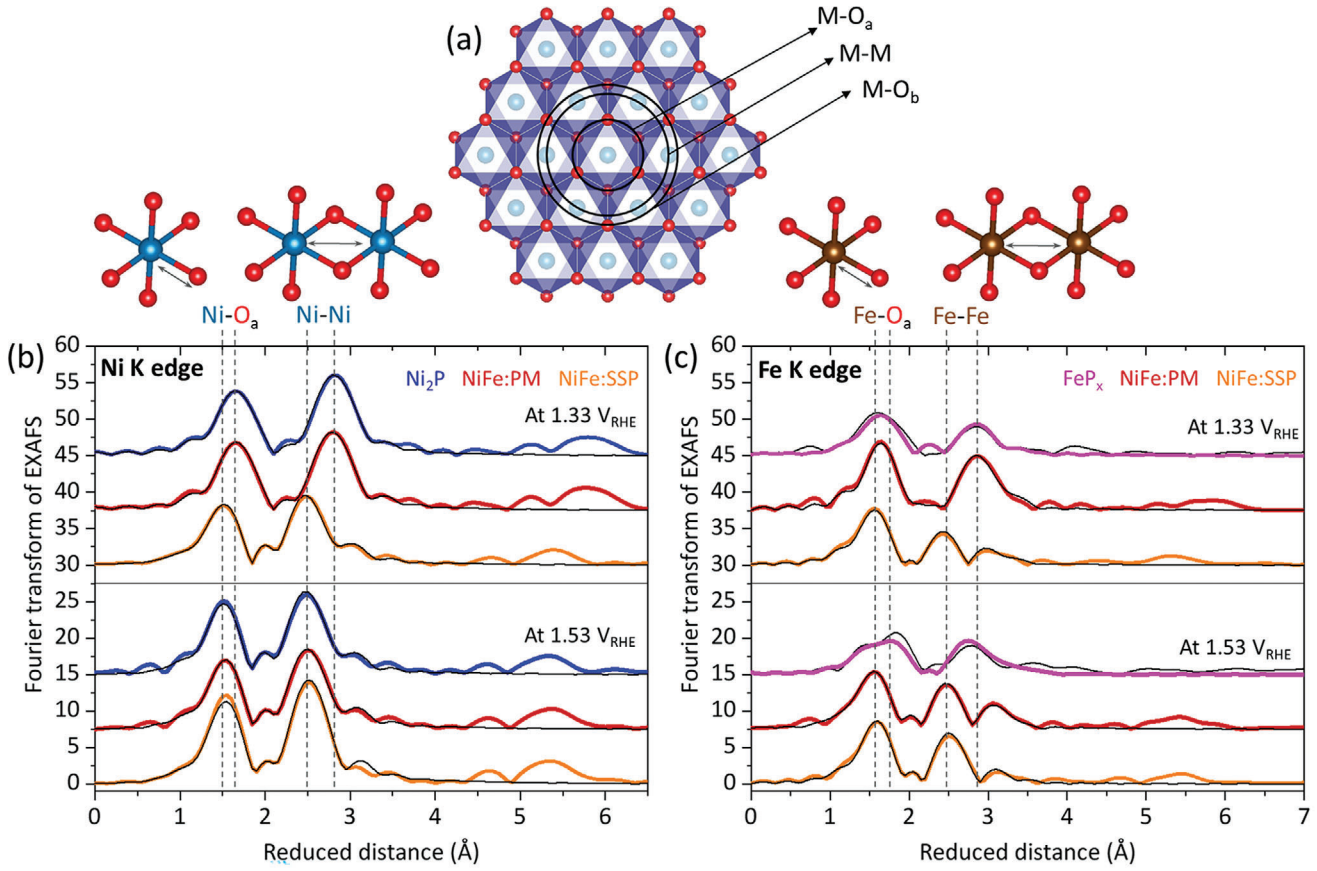

Figure 6. Quasi-in-situ, Fourier-transformed extended X-ray absorption fine structure (EXAFS) data. The k^3-weighted data is shown in Figure S37,S38 (Supporting Information). a) layered model for the oxyhydroxides comprising edge-sharing octahedra. Oxygen atoms are in red and transition metal atoms are in blue. The black rings indicate the three coordination shells used for the simulation of the EXAFS data. Due to the presence of different oxidation states and Jahn-Teller distortion, two distances were used for each of these coordination shells. b) and c) shows the EXAFS data at the Ni and Fe K-edge, respectively, of the four samples after 24 h at 10 mA cm^{-2} and subsequent freeze-quenching at 1.33 or 1.53 V_{RHE}. The simulations are shown as black lines. The simulation's data can be found in Tables S1–S8 (Supporting Information). The two vertical grey dashed lines between 1.5 and 1.7 Å reduced distance represent the short and long distance of the M-O_a coordination shell. The two vertical grey dashed lines between 2.4 and 3.0 Å reduced distance represent the short and long distance of the M-M coordination shell.

reconstruction and phosphorus leaching.[4] In addition to these mappings, TEM bright field images of all four samples have been acquired (Figure 7c–f). They show that the morphologies of the initial samples were not retained, e.g. 20 nm spherical nanoparticles of Ni_2P (Figure 2 for comparison).

3. Discussion and Conclusion

To investigate the effect of heterostructures, electrode substrates, morphology, and reconstruction, we synthesized four different nickel iron phosphide materials (Figure 1 for an overview): crystalline Ni_2P, amorphous FeP_x, a physical mixture of these two (NiFe:PM, Ni to Fe ratio is 2:1), and an amorphous FeP_x matrix with embedded ≈4 nm small, spherical Ni_2P nanoparticles (NiFe:SSP, Ni to Fe ratio is 2:1) via molecular precursor approaches at moderate temperatures. These four materials were deposited on FTO and NF, leading to eight different electrodes. NF, in comparison to FTO, leads to an activity (current density at the same potential) enhancement of around ten times in the Tafel slope regime where mass transport limitations do not significantly contribute (Figure 3). As the Tafel slopes of each material are the same on FTO and NF, the kinds of active sites do not seem to be substantially affected by the substrate. Therefore, we assign the activity enhancement to a higher availability of active sites on NF. Additionally, the NF electrodes show a linear Tafel behavior that expands until higher current densities, suggesting more favorable mass transport properties. An exception to this behavior is FeP_x, whose activity is around 300 times larger on NF compared to FTO. This enormous activity change in comparison to the other samples shows that the NF is not an inert electrode substrate with only a high surface area but chemically interacts with the FeP_x. This chemical interaction is likely the intercalation of iron into the nickel oxyhydroxide that has been shown to form during the OER on NF.[25] Such incorporation phenomena have been well investigated for nickel and iron oxyhydroxides.[43,44] but are still often ignored when iron-containing catalysts are investigated only on seemingly inert NF and no other control substrate.[41,45–47] The activity order of the four compounds on inert FTO is NiFe:SSP>NiFe:PM>Ni_2P>FeP_x (see Note S2, Supporting Information for a brief mechanistic discussion). It is

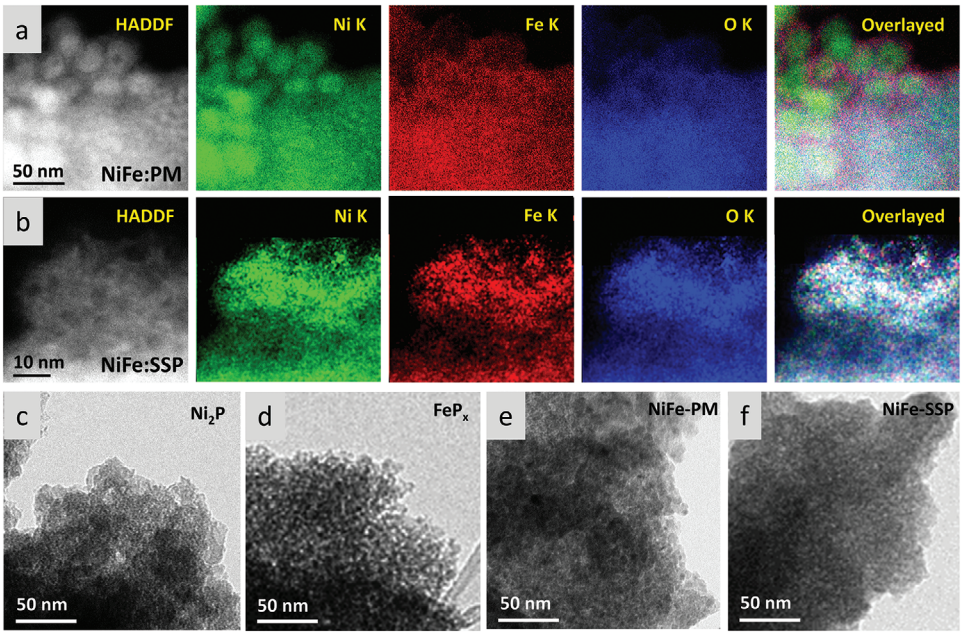

Figure 7. STEM and TEM data of the four herein investigated materials (Figure 1 for naming and synthesis) after 24 h at 10 mA cm^{-2}. A high-angle annular dark field (HAADF) image and the respective elemental mappings are shown in a) for NiFe:PM and b) NiFe:SSP (Figure S40, Supporting Information for the EDX spectra). The data shows that the heterostructure and elemental distribution has been changed severely through the OER treatment (Figure 2 for comparison). c–f) show TEM bright field images of all four samples after 24 h at 10 mA cm^{-2}, showing that the initial morphology has changed severely (Figure 2 for comparison).

tempting to assign the excellent activity of the NiFe:SSP and NiFe:PM heterostructures to an interface effect or the different morphologies, as it has often been done previously.[6–9,20,35,50–52] In this regard, herein, in-situ and post-characterizations have been performed after extended catalytic testing for 24 h. These tests show a fairly stable performance over time, indicating that the oxyhydroxide active sites/structures do not substantially change after their initial formation. However, neither the interfaces between nickel and iron phases nor the morphologies of the precatalysts prevail. The transformation includes not only the often-reported reconstruction into oxyhydroxides,[5] but also the mixing of the iron and nickel phases forming iron-incorporated nickel oxyhydroxides.[53] The previous observation of stable interfaces can be caused by characterizations after short catalytic operation times, as after 30 min, the herein-investigated phosphides also show the prevalence of phosphorus.[6–9,20,35,50–52] These phosphorous amounts are different, showing that the reconstruction is time and precatalyst-dependent. The general observation of the heterostructures instability indicates that interface design between nickel and iron phases for the OER is not straightforwardly achievable and that other explanations for the often observed high activity of non-noble metal OER heterostructures must be found.[9,10,34,35] In this work, we found differences in the distribution of nickel and iron, as a sufficient factor to explain the activity differences of the heterostructures. To find differences in their homogeneity and connect them to the OER activity of the reconstructed phase, in-depth analysis after long reaction times (here 24 h) is required. Iron enhances the OER activity if an ideal amount (20–50%) is incorporated into nickel oxyhydroxide.[29,30,44,48] This incorporation of iron reduces the redox activity of nickel.[29,30,44,48] Thus, when iron and nickel are homogenously distributed and no pure nickel phase is present, a high OER activity and low redox activity is expected. Cyclic voltammetry and in-situ XANES measurements show that the redox activity of the Ni_2P electrode is the highest, followed by NiFe:PM and NiFe:SSP. STEM elemental mappings confirm a more homogenous distribution in NiFe:SSP. Therefore, NiFe:SSP shows a higher activity as most of its oxyhydroxides contain a nickel-to-iron ratio of 1 to 2, which is within the ideal window and NiFe:PM contains too iron and too nickel-rich phases.

This work shows that heterostructured NiFe:SSP is an excellent OER electrode. However, this is not caused by an interface effect between nickel phosphide and iron phosphide or in-situ formed iron oxyhydroxide and nickel oxyhydroxide. It is due to a homogeneous and ideal nickel-iron ratio and high availability of active sites, caused by the 4 nm small precursor particles and the porosity induced by the phosphorus leaching, an effect that has been previously discussed already.[4,54,55] We show that this catalyst can achieve a good performance under industrially relevant conditions (1.51 V_{RHE}, 500 mA cm^{-2}, 6 M KOH, 65 °C, 80 h) and was also suitable for the oxidation of alcohols to ketones. We anticipate that this work underlines how dynamic materials (catalysts) behave under OER conditions and that heterostructures can be outstanding OER electrodes, even though their initial interfaces do not remain, as assumed by previous reports.

Supporting Information

Supporting Information is available from the Wiley Online Library or from the author.

Acknowledgements

This work was funded by the German Federal Ministry of Education and Research (BMBF project "PrometH2eus", 03HY105C) and Deutsche Forschungsgemeinschaft (DFG, German Research Foundation) under Germany's Excellence Strategy – EXC 2008/1 – 390540038 – UniSysCat. STEM analyses were performed on a JEM-ARM300F2, funded by DFG – 403371556 – GZ: INST 131/789-1 FUGG. J.N.H. and P.W.M. greatly acknowledge support from the German Federal Ministry of Education and Research in the project Catlab (03EW0015A/B) framework. H.D. thanks the same ministry for supporting the Live-XAS project (05K22KE1). I.M. was indebted to the SERB Ramanujan fellowship and Alexander von Humboldt postdoctoral fellowship for financial help. K.L. was indebted to the Einstein Foundation Berlin/EC2/BIG-NSE for the Ph.D. fellowship. The authors thank the Helmholtz-Zentrum Berlin (HZB) for beamtime allocation at the KMC-3 synchrotron beamline of the BESSY synchrotron in Berlin-Adlershof and Dr. Ivo Zizak as well as Dr. Michael Haumann for technical support.

Conflict of Interest

The authors declare no conflict of interest.

Author Contributions

J.N.H. and I.M. contributed equally to this work. P.W.M. conceptualized the idea and developed it together with I.M. I.M. performed the electrocatalysis experiments and analyzed all characterizations. S.M. conducted and analyzed XAS measurements while K.L. and I.Z measured Raman spectroscopy. S.K. synthesized the SSPs and V.G. examined organic oxidation reactions. S. S. conducted STEM measurements. J.N.H. wrote the first draft of the paper. H.D., M.D., and P.W.M. supervised the study. All authors discussed the results and commented on the manuscript.

Data Availability Statement

The data that support the findings of this study are available in the supplementary material of this article.

Keywords

FeNiOOH, nickel iron oxyhydroxides, industrial OER conditions, interphase , precatalyst reconstruction

Received: February 20, 2024
Revised: May 18, 2024
Published online: June 6, 2024

[1] IEA, **2019**.
[2] Q. Liang, G. Brocks, A. Bieberle-Hütter, *J. Phys. Energy* **2021**, *3*, 026001.
[3] P. W. Menezes, A. Indra, C. Das, C. Walter, C. Göbel, V. Gutkin, D. Schmeißer, M. Driess, *ACS Catal.* **2017**, *7*, 103.
[4] J. N. Hausmann, P. W. Menezes, *Curr. Opin. Electrochem.* **2022**, *34*, 100991.
[5] B. R. Wygant, K. Kawashima, C. B. Mullins, *ACS Energy Lett.* **2018**, *3*, 2956.
[6] W. Zhang, N. Han, J. Luo, X. Han, S. Feng, W. Guo, S. Xie, Z. Zhou, P. Subramanian, K. Wan, J. Arbiol, C. Zhang, S. Liu, M. Xu, X. Zhang, J. Fransaer, *Small* **2022**, *18*, 2103561.
[7] D. Zheng, L. Yu, W. Liu, X. Dai, X. Niu, W. Fu, W. Shi, F. Wu, X. Cao, *Cell Rep. Phys. Sci.* **2021**, *2*, 100443.
[8] M. Zheng, K. Guo, W.-J. Jiang, T. Tang, X. Wang, P. Zhou, J. Du, Y. Zhao, C. Xu, J.-S. Hu, *Appl. Catal., B* **2019**, *244*, 1004.
[9] D. Bhutani, S. Maity, S. Chaturvedi, D. Chalapathi, U. V. Waghmare, C. Narayana, V. C. Prabhakaran, E. Muthusamy, *J. Mater. Chem. A* **2022**, *10*, 22354.
[10] M. Kuang, J. Zhang, D. Liu, H. Tan, K. N. Dinh, L. Yang, H. Ren, W. Huang, W. Fang, J. Yao, X. Hao, J. Xu, C. Liu, L. Song, B. Liu, Q. Yan, *Adv. Energy Mater.* **2020**, *10*, 2002215.
[11] J. N. Hausmann, P. W. Menezes, *Appl. Catal., B* **2024**, *342*, 123447.
[12] H. Ding, H. Liu, W. Chu, C. Wu, Y. Xie, *Chem. Rev.* **2021**, *121*, 13174.
[13] N. Zhang, R. Jiang, *ChemPlusChem* **2021**, *86*, 1586.
[14] J. Sun, H. Xue, N. Guo, T. Song, Y. Hao, J. Sun, J. Zhang, Q. Wang, *Angew. Chem. Int. Ed.* **2021**, *60*, 19435.
[15] D. Liang, C. Lian, Q. Xu, M. Liu, H. Liu, H. Jiang, C. Li, *Appl. Catal., B* **2020**, *268*, 118417.
[16] Y. Xing, S. Liu, Y. Liu, X. Xiao, Y. Li, Z. Wang, Y. Hu, B. Xin, H. Wang, C. Wang, *Nano Energy* **2024**, *123*, 109402.
[17] C. Ye, Z. Pan, Q. Zhang, F. Yin, Y. Wang, Y. Li, G. Chen, J. Li, Y. Qiu, G. I. N. Waterhouse, L. Gu, Z. Lin, L. Guo, *Energy Environ. Sci.* **2024**, *17*, 332.
[18] F. Nie, Z. Li, X. Dai, X. Yin, Y. Gan, Z. Yang, B. Wu, Z. Ren, Y. Cao, W. Song, *Chem. Eng. J.* **2022**, *431*, 134080.
[19] C. G. Read, J. F. Callejas, C. F. Holder, R. E. Schaak, *ACS Appl. Mater. Interfaces* **2016**, *8*, 12798.
[20] F. Yu, H. Zhou, Y. Huang, J. Sun, F. Qin, J. Bao, W. A. Goddard, S. Chen, Z. Ren, *Nat. Commun.* **2018**, *9*, 2551.
[21] C. Panda, P. W. Menezes, M. Driess, *Angew. Chem., Int. Ed.* **2018**, *57*, 11130.
[22] M. Risch, F. Ringleb, M. Kohlhoff, P. Bogdanoff, P. Chernev, I. Zaharieva, H. Dau, *Energy Environ. Sci.* **2015**, *8*, 661.
[23] J. N. Hausmann, B. Traynor, R. J. Myers, M. Driess, P. W. Menezes, *ACS Energy Lett.* **2021**, *6*, 3567.
[24] M. S. Burke, S. Zou, L. J. Enman, J. E. Kellon, C. A. Gabor, E. Pledger, S. W. Boettcher, *J. Phys. Chem. Lett.* **2015**, *6*, 3737.
[25] J. N. Hausmann, P. V. Menezes, G. Vijaykumar, K. Laun, T. Diemant, I. Zebger, T. Jacob, M. Driess, P. W. Menezes, *Adv. Energy Mater.* **2022**, *12*, 2202098.
[26] S. Lee, L. Bai, X. Hu, *Angew. Chem., Int. Ed.* **2020**, *59*, 8072.
[27] S. Loos, I. Zaharieva, P. Chernev, A. Lißner, H. Dau, *ChemSusChem* **2019**, *12*, 1966.
[28] M. W. Louie, A. T. Bell, *J. Am. Chem. Soc.* **2013**, *135*, 12329.
[29] M. Görlin, P. Chernev, J. Ferreira de Araújo, T. Reier, S. Dresp, B. Paul, R. Krähnert, H. Dau, P. Strasser, *J. Am. Chem. Soc.* **2016**, *138*, 5603.
[30] M. Görlin, J. Ferreira de Araújo, H. Schmies, D. Bernsmeier, S. Dresp, M. Gliech, Z. Jusys, P. Chernev, R. Kraehnert, H. Dau, P. Strasser, *J. Am. Chem. Soc.* **2017**, *139*, 2070.
[31] S. Zou, M. S. Burke, M. G. Kast, J. Fan, N. Danilovic, S. W. Boettcher, *Chem. Mater.* **2015**, *27*, 8011.
[32] A. Dutta, N. Pradhan, *J. Phys. Chem. Lett.* **2017**, *8*, 144.
[33] M. Steimecke, G. Seiffarth, M. Bron, *Anal. Chem.* **2017**, *89*, 10679.
[34] X. Zheng, X. Han, Y. Cao, Y. Zhang, D. Nordlund, J. Wang, S. Chou, H. Liu, L. Li, C. Zhong, Y. Deng, W. Hu, *Adv. Mater.* **2020**, *32*, 2000607.
[35] S. Ni, H. Qu, Z. Xu, X. Zhu, H. Xing, L. Wang, J. Yu, H. Liu, C. Chen, L. Yang, *Appl. Catal., B* **2021**, *299*, 120638.
[36] G. Niaura, A. K. Gaigalas, V. L. Vilker, *J. Phys. Chem. B* **1997**, *101*, 9250.
[37] H.-J. de Jager, L. C. Prinsloo, *Thermochim. Acta* **2001**, *376*, 187.
[38] E. M. Oliveira, M. Rogero, E. C. Ferreira, J. A. Gomes Neto, *Spectrochim. Acta, Part A* **2021**, *246*, 119025.
[39] N. Zhang, Y. Hu, L. An, Q. Li, J. Yin, J. Li, R. Yang, M. Lu, S. Zhang, P. Xi, C. Yan, *Angew. Chem., Int. Ed.* **2022**, *61*, 2207217.

[40] D. Friebel, M. W. Louie, M. Bajdich, K. E. Sanwald, Y. Cai, A. M. Wise, M.-J. Cheng, D. Sokaras, T.-C. Weng, R. Alonso-Mori, R. C. Davis, J. R. Bargar, J. K. Nørskov, A. Nilsson, A. T. Bell, *J. Am. Chem. Soc.* **2015**, *137*, 1305.
[41] J. N. Hausmann, R. Beltrán-Suito, S. Mebs, V. Hlukhyy, T. F. Fässler, H. Dau, M. Driess, P. W. Menezes, *Adv. Mater.* **2021**, *33*, 2008823.
[42] R. Beltrán-Suito, V. Forstner, J. N. Hausmann, S. Mebs, J. Schmidt, I. Zaharieva, K. Laun, I. Zebger, H. Dau, P. W. Menezes, M. Driess, *Chem. Sci.* **2020**, *11*, 11834.
[43] D. Y. Chung, P. P. Lopes, P. Farinazzo Bergamo Dias Martins, H. He, T. Kawaguchi, P. Zapol, H. You, D. Tripkovic, D. Strmcnik, Y. Zhu, S. Seifert, S. Lee, V. R. Stamenkovic, N. M. Markovic, *Nat. Energy* **2020**, *5*, 222.
[44] L. Trotochaud, S. L. Young, J. K. Ranney, S. W. Boettcher, *J. Am. Chem. Soc.* **2014**, *136*, 6744.
[45] J. Hu, S. Li, J. Chu, S. Niu, J. Wang, Y. Du, Z. Li, X. Han, P. Xu, *ACS Catal.* **2019**, *9*, 10705.
[46] S. Niu, W.-J. Jiang, Z. Wei, T. Tang, J. Ma, J.-S. Hu, L.-J. Wan, *J. Am. Chem. Soc.* **2019**, *141*, 7005.
[47] D. Zhong, L. Liu, D. Li, C. Wei, Q. Wang, G. Hao, Q. Zhao, J. Li, *J. Mater. Chem. A* **2017**, *5*, 18627.
[48] F. Dionigi, Z. Zeng, I. Sinev, T. Merzdorf, S. Deshpande, M. B. Lopez, S. Kunze, I. Zegkinoglou, H. Sarodnik, D. Fan, A. Bergmann, J. Drnec, J. F. de Araujo, M. Gliech, D. Teschner, J. Zhu, W.-X. Li, J. Greeley, B. R. Cuenya, P. Strasser, *Nat. Commun.* **2020**, *11*, 2522.
[49] F. Dionigi, J. Zhu, Z. Zeng, T. Merzdorf, H. Sarodnik, M. Gliech, L. Pan, W. Li, J. Greeley, P. Strasser, *Angew. Chem., Int. Ed.* **2021**, *60*, 14446.
[50] Y. Du, B. Li, G. Xu, L. Wang, *InfoMat* **2023**, *5*, 12377.
[51] P. Zhai, C. Wang, Y. Zhao, Y. Zhang, J. Gao, L. Sun, J. Hou, *Nat. Commun.* **2023**, *14*, 1873.
[52] F. Song, M. M. Busch, B. Lassalle-Kaiser, C.-S. Hsu, E. Petkucheva, M. Bensimon, H. M. Chen, C. Corminboeuf, X. Hu, *ACS Cent. Sci.* **2019**, *5*, 558.
[53] M. Görlin, P. Chernev, P. Paciok, C.-W. Tai, J. Ferreira de Araújo, T. Reier, M. Heggen, R. Dunin-Borkowski, P. Strasser, H. Dau, *Chem. Commun.* **2019**, *55*, 818.
[54] J. N. Hausmann, S. Mebs, K. Laun, I. Zebger, H. Dau, P. W. Menezes, M. Driess, *Energy Environ. Sci.* **2020**, *13*, 3607.
[55] Y. Hu, Y. Zheng, J. Jin, Y. Wang, Y. Peng, J. Yin, W. Shen, Y. Hou, L. Zhu, L. An, M. Lu, P. Xi, C.-H. Yan, *Nat. Commun.* **2023**, *14*, 1949.